30th AIAA Applied Aerodynamics Conference
25 - 28 June 2012, New Orleans, Louisiana

AIAA 2012-3327

Unsteady Aerodynamics Modeling for Aircraft Maneuvers: a New Approach Using Time-Dependent Surrogate Modeling

Mehdi Ghoreyshi*and Russell M. Cummings†
Modeling and Simulation Research Center, U.S. Air Force Academy
USAF Academy, Colorado 80840-6400

A new approach for computing the unsteady and nonlinear aerodynamic loads acting on a maneuvering aircraft is presented. This approach is based on Duhamel's superposition integral using indicial (step) response functions. The novelty of this approach relies on the development of a time-dependent surrogate model that fits the relationship between flight conditions (Mach number and angle of attack) and indicial functions calculated from a limited number of simulations (samples). The aircraft studied in the current paper exhibit highly nonlinear roll moment and therefore a very large number of step functions need to be calculated to accurately predict the aerodynamic behavior at each instant of time spent in aircraft maneuvers. The reduced order model, along with the surrogate model, provide a mean for rapid calculation of step functions and predicting aerodynamic forces and moments during maneuvering flight. The maneuvers are generated using a time-optimal prediction code with the feasible solutions based on the vehicle control and state constraints. Results presented show that the developed surrogate model aids in reducing the overall computational cost to develop cost-effective reduced-order models. It is also demonstrated that the reduced order model used can accurately predict time-marching solutions of maneuvering aircraft, but with an advantage that reduced order model predictions only require on the order of a few seconds of computational time.

I. Introduction

The use of Computational Fluid Dynamics (CFD) simulations during the preliminary aircraft design phase has been continuously increasing because the unsteady aerodynamic characteristics can have a significant effect on the aircraft calculated stability and control characteristics.[1] Despite their greatest efforts using the best available predictive capabilities, nearly every major fighter program since 1960 has had costly nonlinear aerodynamic or fluid-structure interaction issues that were not discovered until flight testing.[2] Some recent aircraft experiencing unexpected characteristics are the F/A-18, F-18E, and F-22.[2,3] The lack of full understanding of unsteady aerodynamics typically leads to "cut and try" efforts, which result in very expensive and time-consuming solutions.[4] The CFD tools have become credible for the computation of aerodynamics experienced by a maneuvering fighter with time history effects and hence would help to reduce the amount of wind tunnel and flight testing. At the highest practical level, a full-order aerodynamic model can be developed based on the direct solution of the discretized Reynolds-Averaged Navier-Stokes (RANS) equations coupled with the dynamic equations governing aircraft motion.[5] First attempts at this approach were limited to two-dimensional test cases, while with recent advances in computing techniques and the capabilities provided by high performance computing resources, the coupled CFD-flight dynamics of a full aircraft has been studied.[6,7] The full-order modeling is an infinite-dimensional problem because the solution at each time depends on all of the states at times prior to the current state and the flow equations describe the motion of the fluid at infinitely many points.[5,8] Also, the high computational cost associated with this type of simulation for stability and control analysis still remains a challenging problem. For example,

*NRC Research Fellow, AIAA Senior Member
†Professor of Aeronautics, AIAA Associate Fellow

researchers at NASA Ames have attempted to perform a "brute force" approach to filling a stability and control database for vehicle design. They found that a reasonable database for static stability and control derivatives would include on the order of 30 different angles-of-attack, 20 different Mach numbers, and 5 different side-slip angles, each for a number of different geometry configurations or control surface deflections.[9] They estimated that filling this database would conservatively require 10,000 to 20,000 static CFD runs, and this approach does not address the dynamic stability characteristics of the aircraft. Using CFD in this way is therefore unrealistic.

To make timely progress in the use of CFD for aircraft design, the efforts over the last few years have been spent mainly on the development of a Reduced Order Model (ROM) using CFD from an appropriate training maneuver(s) and an accurate System IDentification (SID) approach.[10–12] The objective of the ROMs is to develop a model that significantly reduces the CFD simulation time required to create a full aerodynamics database, making it possible to accurately model aircraft static and dynamic characteristics from a number of time-accurate CFD simulations. Recent efforts on the development of ROMs can be classified into two types: time domain or frequency domain approaches.[13] The frequency domain models are obtained from matching transfer functions computed from the measured input-output data.[14] Examples of the frequency domain ROMs are the indicial response method by Ballhaus and Goorjian[15] and Tobak et al.,[16,17] and a frequency-domain approach based on proper orthogonal decomposition by Hall.[18] Some examples of time domain ROMs include the unit sample response by Gaitonde and Jones,[19] Volterra theory by Silva and Bartels,[20] Radial Basis Functions (RBF)[21] and state-space modeling.[22] The current paper aims to assess the accuracy of prediction of reduced order models based on the indicial response theory.

The transient aerodynamic response due to a step change in a forcing parameter, such as angle of attack or pitch rate is a so-called "indicial function". Assuming that the indicial functions are known, the aerodynamic forces and moments induced in any maneuver can be estimated by using the well-known Duhamel's superposition integral.[23] Although, the indicial functions are used as a fundamental approach to represent the unsteady aerodynamic loads, there is only limited report of using these functions for aerodynamics modeling of three-dimensional configurations. Experimental tests are practically nonexistent for indicial function measurements due to wind tunnel constraints. Limited analytical expressions of indicial functions exist for two-dimensional airfoils.[24] However, these analytical expressions are not valid for aircraft configurations due to the three-dimensional tip vortices. The only direct method for determination of response functions is using CFD.[25]

Recently, the CFD solutions for the indicial response of airfoils and wings have been reported (see for example, Manglano-Villamarin and Shaw,[26] Singh and Baeder[27] and Raveh[28]). Also, Ghoreyshi et al.[25] described an approach based on a grid motion technique for CFD-type calculation of linear and nonlinear inidical functions with respect to angle of attack and pitch rate. Ghoreyshi and Cummings[29] later used this approach to generate linear indicial functions due to longitudinal and lateral forcing parameters of a generic unmanned combat air vehicle (UCAV) and used these functions for predicting the aerodynamic responses to aircraft six degrees of freedom maneuvers. They showed that while lift, side-force and pitch moment match quite well with full-order simulations in the linear regime but the roll and yaw moments do not match even at low angles of attack. For the vehicle studied, the roll and yaw moment variation with the angle of attack and Mach number is highly nonlinear. The objective of this paper is to extend the ROM to include the effects of angle of attack and Mach number in the indicial functions.

Having a ROM to predict the aerodynamic responses to any arbitrary motion over a wide flight regime could become a very expensive approach because a large number of indicial functions need to be computed for each combination of angle of attack and free-stream Mach number. Typically, the CFD simulation of indicial functions start from a steady state solution and are marched (iterated) in pseudo time within each physical time step using a dual-time stepping scheme. The generation of all response functions in the angle of attack/Mach number space using CFD is therefore expensive and makes the creation of a ROM very time consuming. Note that these models are still cheaper than full-order simulations because the ROMs based on indicial functions eliminate the need to repeat calculations for each frequency. In this paper, a surrogate model is proposed based on the Kriging technique[30] to model indicial functions for a new flight conditions from available (observed) responses. These observed responses are viewed as a set of time-correlated spatial processes where the output is considered a time-dependent function.

The main objective of the present study is to develop a reduced order model based on Duhamel's superposition integral using indicial (step) response functions for computing the aerodynamic loads acting on a maneuvering aircraft. The indicial functions include longitudinal and lateral forces and moments and are directly calculated using unsteady RANS simulations with a prescribed grid motion. A method to efficiently reduce the number of indicial response calculations is proposed. This method uses a time-dependent surrogate model to fit the relationship between flight conditions and response functions from a limited number of response simulations (samples). The six-degree-of-freedom (6-DOF) aerodynamics model is then created with predicted indicial functions at each time instant using the developed surrogate model. The model will then be evaluated for two generated maneuvers, which were replayed directly through an unsteady CFD simulation. The maneuvers were defined using a time optimal control solver.

II. Formulation

A. CFD Solver

The flow solver used for this study is the *Cobalt* code[31] that solves the unsteady, three-dimensional and compressible Navier-Stokes equations in an inertial reference frame. These equations in integral form are[32]

$$\frac{\partial}{\partial t}\iiint \mathbf{Q}dV + \iint(\mathbf{f}\hat{\imath} + \mathbf{g}\hat{\jmath} + \mathbf{h}\hat{k}).\hat{n}dS = \iint(\mathbf{r}\hat{\imath} + \mathbf{s}\hat{\jmath} + \mathbf{t}\hat{k}).\hat{n}dS \tag{1}$$

where V is the fluid element volume; S is the fluid element surface area; $\hat{n}$ is the unit normal to S; $\hat{\imath}$, $\hat{\jmath}$, and $\hat{k}$ are the Cartesian unit vectors; $\mathbf{Q} = (\rho, \rho u, \rho v, \rho w, \rho e)^T$ is the vector of conserved variables, where ρ represents air density, u, v, w are velocity components and e is the specific energy per unit volume. The vectors of $\mathbf{f}$, $\mathbf{g}$, and $\mathbf{h}$ represent the inviscid components and are detailed below

$$\begin{aligned} \mathbf{f} &= (\rho u, \rho u^2 + p, \rho uv, \rho uw, u(\rho e + p))^T \\ \mathbf{g} &= (\rho v, \rho v^2 + p, \rho vu, \rho vw, v(\rho e + p))^T \\ \mathbf{h} &= (\rho w, \rho w^2 + p, \rho wv, \rho wv, w(\rho e + p))^T \end{aligned} \tag{2}$$

where the superscript T denotes the transpose operation. The vectors of $\mathbf{r}$, $\mathbf{s}$, and $\mathbf{t}$ represent the viscous components which are described as

$$\begin{aligned} \mathbf{r} &= (0, \tau_{xx}, \tau_{xy}, \tau_{xz}, u\tau_{xx} + v\tau_{xy} + w\tau_{xz} + kT_x)^T \\ \mathbf{s} &= (0, \tau_{xy}, \tau_{yy}, \tau_{yz}, u\tau_{xy} + v\tau_{yy} + w\tau_{yz} + kT_y)^T \\ \mathbf{t} &= (0, \tau_{xz}, \tau_{zy}, \tau_{zz}, u\tau_{xz} + v\tau_{zy} + w\tau_{zz} + kT_z)^T \end{aligned} \tag{3}$$

where τ_{ij} are the viscous stress tensor components, T is the temperature, and k is the thermal conductivity. The ideal gas law and Sutherland's law closes the system of equations and the entire equation set is nondimensionalized by free stream density and speed of sound.[31] The Navier-Stokes equations are discretised on arbitrary grid topologies using a cell-centered finite volume method. Second-order accuracy in space is achieved using the exact Riemann solver of Gottlieb and Groth,[33] and least squares gradient calculations using QR factorization. To accelerate the solution of discretized system, a point-implicit method using analytic first-order inviscid and viscous Jacobians. A Newtonian sub-iteration method is used to improve time accuracy of the point-implicit method. Tomaro et al.[34] converted the code from explicit to implicit, enabling Courant-Friedrichs-Lewy numbers as high as 10^6. The *Cobalt* solver has been used at the Air Force Seek Eagle Office (AFSEO) and the United States Air Force Academy (USAFA) for a variety of unsteady nonlinear aerodynamic problems of maneuvering aircraft.[35–39]

B. Indicial Theory

The mathematical models of using indicial responses for modeling unsteady aerodynamics of a maneuvering aircraft were detailed by Ghoreyshi and Cummings.[29] In this model, the response functions were generated at different free-stream Mach numbers. In this paper, a more general approach is used where the responses in the angle of attack and side-slip depend on both the angle of attack and Mach number. It is assumed that the indicial functions with respect to the angular rates change with changes in free-stream Mach number but do not vary with the changes in angle of attack for the maneuvers studied. In this approach, the time responses in lift due to the step changes in angle of attack, α, and normalized pitch rate, q, are denoted as $C_{L\alpha}$ and C_{Lq}, respectively. The unsteady lift coefficient at time t is obtained as:

$$C_L(t) = C_{L0}(M) + \frac{d}{dt}\left[\int_0^t C_{L\alpha}(t-\tau,\alpha,M)\alpha(\tau)d\tau\right] + \frac{d}{dt}\left[\int_0^t C_{Lq}(t-\tau,M)q(\tau)d\tau\right] \tag{4}$$

where, C_{L0} denote the zero-angle of attack lift coefficient and is found from static calculations; M denotes the free-stream Mach number. Note that the indicial response function with respect to the rate of change of velocity, i.e. $\dot{V}$ are assumed small and are not modeled. Likewise, the time responses in pitch moment due to the step changes in α, and q, are denoted as $C_{m\alpha}$ and C_{mq} and then the pitch moment is estimated as follows:

$$C_m(t) = C_{m0}(M) + \frac{d}{dt}\left[\int_0^t C_{m\alpha}(t-\tau,\alpha,M)\alpha(\tau)d\tau\right] + \frac{d}{dt}\left[\int_0^t C_{mq}(t-\tau,M)q(\tau)d\tau\right] \tag{5}$$

The unsteady effects in drag force are assumed to be small and therefore are not discussed here. The response function due to pitch rate, i.e. $C_{jq}(M)$ for $j = L, m$ can be estimated using a time-dependent interpolation scheme from the observed responses. This value is next used to estimate the second integrals in Eqs. 4 and 5, however, the estimation of the integral with respect to the angle of attack needs more explanation. Assuming a set of angle of attack samples of $\alpha = [\alpha_1, \alpha_2, ..., \alpha_n]$ at free-stream Mach numbers of $M = [M_1, M_2, ..., M_m]$, the pitch moment response to each angle of $\alpha_i, i = 1, 2, ..., n$ at Mach number of $M_j, j = 1, 2, ..., m$ is denoted as $A_\alpha(t, \alpha_i, M_j)$. In these response simulations, $\alpha(t) = 0$ at $t = 0$ and is held constant at α_i for all $t > 0$. For a new angle of $\alpha^* > 0$ at a new free-stream Mach number of M^*, the responses of $A_\alpha(t, \alpha_k, M^*)$ are being interpolated at $\alpha_k = [\alpha_1, \alpha_2, ..., \alpha_s]$, such that $0 < \alpha_1 < \alpha_2 < ... < \alpha_s$ and $\alpha_s = \alpha^*$. These angles can have a uniform or non-uniform spacing. The indicial functions of $C_{j\alpha_k}$ for $k = 1, ..., s$ at each interval of $[\alpha_{k-1}, \alpha_k]$ are defined as

$$C_{j\alpha_1} = \frac{A_\alpha(t,\alpha_1,M^*) - C_{j0}(M^*)}{\alpha_1} \tag{6}$$

$$C_{j\alpha_k} = \frac{A_\alpha(t,\alpha_k,M^*) - A_\alpha(t,\alpha_{k-1},M^*)}{\alpha_k - \alpha_{k-1}} \tag{7}$$

where C_{j0} denotes the zero angle of attack pitch moment coefficient. The interval indicial functions are then used to estimate the values of first integrals in Eqs. 4 and 5. These steps can easily be followed for a negative angle of attack, i.e. $\alpha^* < 0$. Assuming that the lateral loads only depend on side-slip angle (β), normalized roll rate (p), and normalized yaw rate (r), the unsteady lateral forces and moments using indicial functions are written as:

$$\begin{aligned} C_Y(t) = &\frac{d}{dt}\left[\int_0^t C_{Y\beta}(t-\tau,\alpha,M)\beta(\tau)d\tau\right] + \frac{d}{dt}\left[\int_0^t C_{Yp}(t-\tau,M)p(\tau)d\tau\right] + \\ &\frac{d}{dt}\left[\int_0^t C_{Yr}(t-\tau,M)r(\tau)d\tau\right] \end{aligned} \tag{8}$$

$$\begin{aligned} C_l(t) = &\frac{d}{dt}\left[\int_0^t C_{l\beta}(t-\tau,\alpha,M)\beta(\tau)d\tau\right] + \frac{d}{dt}\left[\int_0^t C_{lp}(t-\tau,M)p(\tau)d\tau\right] + \\ &\frac{d}{dt}\left[\int_0^t C_{lr}(t-\tau,M)r(\tau)d\tau\right] \end{aligned} \tag{9}$$

$$\begin{aligned} C_n(t) = &\frac{d}{dt}\left[\int_0^t C_{n\beta}(t-\tau,\alpha,M)\beta(\tau)d\tau\right] + \frac{d}{dt}\left[\int_0^t C_{np}(t-\tau,M)p(\tau)d\tau\right] + \\ &\frac{d}{dt}\left[\int_0^t C_{nr}(t-\tau,M)r(\tau)d\tau\right] \end{aligned} \tag{10}$$

where, C_Y, C_l and C_n denote the side-force, roll and yaw moments, respectively. The functions of $C_{L\alpha}(t,\alpha,M)$, $C_{m\alpha}(t,\alpha,M)$, $C_{Lq}(t,M)$, $C_{mq}(t,M)$, $C_{Y\beta}(t,\alpha,M)$, $C_{l\beta}(t,\alpha,M)$, $C_{n\beta}(t,\alpha,M)$, $C_{Yp}(t,M)$, $C_{lp}(t,M)$, $C_{np}(t,M)$, $C_{Yr}(t,M)$, $C_{lr}(t,M)$, and $C_{nr}(t,M)$ are unknown and will be determined in this paper using CFD with a grid movement tool, along with a time-dependent surrogate model.

C. Surrogate-Based Modeling of Indicial Functions

Having a ROM to predict the aerodynamic responses to any arbitrary motion over a wide flight regime could become a very expensive approach because a large number of indicial functions needs to be computed. In order to achieve a reasonable computational cost, a special time-dependent surrogate-based modeling approach is adapted to predict indicial responses for a new point from available (observed) responses. These observed responses are viewed as a set of time-correlated spatial processes where the output is considered a time-dependent function. Romero et al.[40] developed a framework for multi-stage Bayesian surrogate models for the design of time dependent systems and tested their model for free vibrations of a mass-spring-damper system assuming the input parameters of stiffness and damping factor at different initial conditions. This framework is examined for reduced order modeling of nonlinear and unsteady aerodynamic loads. Assume an input vector of $\mathbf{x}(t) = \big(x_1(t), x_2(t), ..., x_n(t)\big)$ where n represents the dimensionality of the input vector. To construct a surrogate model for fitting the input-output relationship, the unsteady aerodynamic responses corresponding to a limited number of input parameters (training parameters or samples) need to be generated. Design of Experiment methods, for example, can be used to select m samples from the input space. The input matrix $\mathbf{D}(m \times n)$ is then defined as:

$$\mathbf{D} = \begin{bmatrix} x_{11} & x_{12} & \cdots & x_{1n} \\ x_{21} & x_{22} & \cdots & x_{2n} \\ \vdots & \vdots & \vdots & \vdots \\ x_{m1} & x_{m2} & \cdots & x_{mn} \end{bmatrix} \tag{11}$$

where rows correspond to different combinations of the design parameters. For each row in the input matrix, a time-dependent response was calculated at p discrete values of time, and this information is summarized in the output matrix of $\mathbf{Z}(m \times p)$ as:

$$\mathbf{Z} = \begin{bmatrix} y_{11} & y_{12} & \cdots & y_{1p} \\ y_{21} & y_{22} & \cdots & y_{2p} \\ \vdots & \vdots & \vdots & \vdots \\ y_{m1} & y_{m2} & \cdots & y_{mp} \end{bmatrix} \tag{12}$$

where for aerodynamic loads modeling, p equals the number of iterations used in time-marching CFD calculations. The objective of surrogate modeling is to develop a model that allows predicting the aerodynamic response of $\mathbf{y}(\mathbf{x_0}) = \big(y_{01}, y_{02}, ..., y_{0p}\big)$ at a new combination of input parameter of $\mathbf{x_0}$. To construct this surrogate model, the responses at each time step are assumed as a separate set, such that each column of the output matrix is a partial realization of the total response. In this sense, p surrogate models are created; they are denoted as $\mathbf{Z_i}(\mathbf{D})$ for $i = 1, 2, ..., p$. A universal-type Kriging function[30] is used to approximate these models. Each $\mathbf{Z_i}(\mathbf{D})$ function can be approximated as the sum of a deterministic mean (trend), μ and a zero-mean spatial random process, ϵ with a given covariance structure of σ^2, therefore each function value at the new sample of $\mathbf{x_0}$ is

$$\tilde{\mathbf{Z}}_{\mathbf{i}}(\mathbf{x_0}) = \mu + \epsilon \tag{13}$$

where, the tilde accent shows that surrogate model is an approximation of the actual function. Universal Kriging, which is used in this paper, assumes that the mean value μ is a linear combination of known regression functions of $\mathbf{f}_0(x), \mathbf{f}_1(x), .., \mathbf{f}_n(x)$. In this paper, the linear functions are used, therefore, $\mathbf{f}_0(x) = 1$ and $\mathbf{f}_j(x) = x_j$ for $j = 1, 2, ..., n$. This changes Eq. (13) as:

$$\tilde{\mathbf{Z}}_{\mathbf{i}}\left(\mathbf{x_0}\right)=\sum_{j=0}^{n}\beta_{ij}\mathbf{f}_j\left(\mathbf{x_0}\right)+\epsilon \tag{14}$$

where β_{ij} represent the regression coefficient for the j-th regression function of response function at time step i, $i=1,2,...,p$. To estimate the spatial random process of ϵ, a spatially weighted distance formula is defined between samples given in matrix $\mathbf{D}$ such that for sample $\mathbf{x}_i$ and $\mathbf{x}_j$, the distance is written as:

$$d\left(\mathbf{x}_i,\mathbf{x}_j\right)=\sum_{h=1}^{n}\theta_h\left|x_h^{(i)}-x_h^{(j)}\right|^{p_h}\quad(\theta_h\geq 0\text{ and }p_h\in[0,1]) \tag{15}$$

where $|.|$ shows the Euclidean distance; the parameter θ_h expresses the importance of the h-th component of the input vector, and the exponent p_h is related to the smoothness of the function in coordinate direction h. A correlation matrix $\mathbf{R}(m\times m)$ with a Gaussian spatial random process is then defined as:

$$\mathbf{R}=\begin{bmatrix}\exp\left[-\frac{d(\mathbf{x}_1,\mathbf{x}_1)}{\sigma^2}\right] & \exp\left[-\frac{d(\mathbf{x}_1,\mathbf{x}_2)}{\sigma^2}\right] & \cdots & \exp\left[-\frac{d(\mathbf{x}_1,\mathbf{x}_m)}{\sigma^2}\right]\\ \vdots & \vdots & \vdots & \vdots\\ \exp\left[-\frac{d(\mathbf{x}_m,\mathbf{x}_1)}{\sigma^2}\right] & \exp\left[-\frac{d(\mathbf{x}_m,\mathbf{x}_2)}{\sigma^2}\right] & \cdots & \exp\left[-\frac{d(\mathbf{x}_m,\mathbf{x}_m)}{\sigma^2}\right]\end{bmatrix} \tag{16}$$

To compute the Kriging model, values must be estimated for β_{ij}, σ, θ_h, and p_h. These parameters can be quantified using the maximum likelihood estimator, as described by Jones et al.[41] Next the vector of $\mathbf{R}(m\times 1)$ is defined from correlations between the new design parameter $\mathbf{x_0}$ and the m sample points, based on the distance formula in Eq. (15), i.e.

$$\mathbf{r}=\begin{bmatrix}\exp\left[-\frac{d(\mathbf{x}_1,\mathbf{x}_0)}{\sigma^2}\right]\\ \exp\left[-\frac{d(\mathbf{x}_2,\mathbf{x}_0)}{\sigma^2}\right]\\ \vdots\\ \exp\left[-\frac{d(\mathbf{x}_m,\mathbf{x}_0)}{\sigma^2}\right]\end{bmatrix} \tag{17}$$

and now $\tilde{\mathbf{Z}}_{\mathbf{i}}\left(\mathbf{x_0}\right)$ can be estimated as

$$\tilde{\mathbf{Z}}_{\mathbf{i}}\left(\mathbf{x_0}\right)=\sum_{j=0}^{n}\beta_{ij}\mathbf{f}_j\left(\mathbf{x_0}\right)+\mathbf{r}^T\mathbf{R}^{-1}\left(\mathbf{Z}_{\mathbf{i}}\left(\mathbf{D}\right)-\mathbf{F}\beta\right) \tag{18}$$

where, β is the $n+1$ dimensional vector of regression coefficients; $\mathbf{Z}_{\mathbf{i}}\left(D\right)$ is the observed responses at time step i, $i=1,2,...,p$ and matrix $\mathbf{F}$ is

$$\mathbf{F}=\begin{bmatrix}\mathbf{f_0}\left(x_1\right) & \mathbf{f_1}\left(x_1\right) & \cdots & \mathbf{f_n}\left(x_1\right)\\ \vdots & \vdots & \vdots & \vdots\\ \mathbf{f_0}\left(x_m\right) & \mathbf{f_1}\left(x_m\right) & \cdots & \mathbf{f_n}\left(x_m\right)\end{bmatrix} \tag{19}$$

The total response at $\mathbf{x_0}$ is then combination of predicted values of each surrogate model, i.e.

$$\tilde{\mathbf{Z}}\left(\mathbf{x_0}\right)=\left(\tilde{\mathbf{Z}}_{\mathbf{1}}\left(\mathbf{x_0}\right),\tilde{\mathbf{Z}}_{\mathbf{2}}\left(\mathbf{x_0}\right),...,\tilde{\mathbf{Z}}_{\mathbf{p}}\left(\mathbf{x_0}\right)\right) \tag{20}$$

D. CFD Calculation of Indicial Functions

Limited analytical expressions of indicial functions exist for two-dimensional airfoils.[24] For incompressible flows, Wagner[42] was the first who detailed the analytical unsteady lift of a thin airfoil undergoing a plunging motion using a single indicial function (the so-called Wagner's function) with its exact values defined in terms of Bessel functions. His function was approximated in non-dimensional time by a two-pole exponential function as[43]

$$C_{L\alpha} = 1 - 0.165\exp(-0.0455s) - 0.33\exp(-0.3s) \tag{21}$$

where $s = 2Vt/c$ is the normalized time. Note that Wagner's function is valid only for low speed flows and the times after the initial disturbance. Lomax[44] later used the linearized Euler equations to derive exact initial values of the compressible indicial response of a flat plate airfoil to a step change in the angle of attack, and his equation was expressed as:

$$C_{L\alpha} = \frac{4}{M}\left(1 - \frac{1-M}{2M}s\right) \tag{22}$$

where M is the Mach number. However, these analytical expressions are not valid for aircraft configurations due to three-dimensional tip vortices. An alternative is to use CFD, but special considerations are required to simulate step responses in CFD. Singh and Baeder[27] used a surface transpiration approach to directly calculate the angle of attack indicial response using CFD. Ghoreyshi et al.[25] also described an approach based on a grid motion technique for CFD-type calculation of linear and nonlinear inidical functions. In this paper, the indicial functions due to longitudinal and lateral forcing parameters (angle of attack, side-slip angle, and angular rates) are calculated using CFD and the grid motion approach.

Cobalt uses an arbitrary Lagrangian-Eulerian formulation and hence allows all translational and rotational degrees of freedom.[25] The code can simulate both free and specified six degree of freedom (6DoF) motions. The rigid motion is specified from a motion input file. For the rigid motion the location of a reference point on the aircraft is specified at each time step. In addition the rotation of the aircraft about this reference point is also defined using the rotation angles of yaw, pitch and roll (bank). The aircraft reference point velocity, v_a, in an inertial frame is then calculated to achieve the required angles of attack and sideslip, and the forward speed. The velocity is then used to calculate the location. The initial aircraft velocity, v_0, is specified in terms of Mach number, angle of attack and side-slip angle in the main file. The instantaneous aircraft location for the motion file is then defined from the relative velocity vector, $v_a - v_0$. For CFD-type calculation of a step change in angle of attack, the grid immediately starts to move at $t = 0$ to the right and downward as shown in Fig. 1. The translation continues over time with a constant velocity vector. Since there is no rotation, all the effects in aerodynamic loads are from changes in the angle of attack. For a unit step change in pitch rate, the grid moves and rotates simultaneously. The grid starts to rotate with a unit pitch rate at $t = 0$. To hold the angle of attack zero during the rotation, the grid moves right and upward in Fig. 1.

E. Time Optimal Maneuvers

An optimal control approach[45,46] is used to generate 6-DOF maneuvers for a generic UCAV with the feasible solutions based on the vehicle control and state constraints. This approach finds the optimal controls that transfer a system from the initial state to the final state while minimizing (or maximizing) a specified cost function.[47] The optimal control aims to find a state-control pair $x^*(), u^*()$ and possibly the final event time t_f that minimizes the cost function

$$J[x(), u(), t_0, t_f] = E(x(t_0), u(t_f), t_0, t_f) + \int_{t_0}^{t_f} F(x(t), u(t), t)dt \tag{23}$$

where $x \in R^n$ and $u \in R^m$. The function E and F are endpoint cost and Lagrangian (running cost), respectively. The minimization is subject to the dynamic constraint,

$$\dot{x}(t) = f(x(t), u(t)), \qquad t \in [t_0, t_f] \tag{24}$$

and boundary conditions

$$\psi_0[x(t_0), t_0] = 0 \tag{25}$$

$$\psi_f[x(t_f), t_f] = 0 \tag{26}$$

where $\psi_0 \in R^p$ and $\psi_f \in R^q$ with $p, q \leq n$. These boundary conditions are fixed with trimmed flight conditions, but the rest of the maneuver is an out-of-trim condition. There are many different methods of solving the optimal control problems; the optimal control solver of DIDO[48] is used here. Note that DIDO is not actually an acronym; the method is named for Queen Dido of Carthage who was the first person known to have solved a dynamic optimization problem. This code has been widely used and tested for aircraft optimal control problem. In DIDO, the total time history is divided into N segments, spaced using a shifted Legendre-Gauss-Lobatto (LGL) rule.[49,50] The boundaries of each time segment are called nodes. The code exploits Pseudo-Spectral (PS) methods for solving the optimal control problems. For the problem of an aircraft optimal time maneuver, the general 6-DOF aircraft equations of motion detailed in Etkin[51] serve as one of the constraints. The aircraft state vector consists of the position of the aircraft (x, y, z), the standard Euler angles (ϕ, θ, ψ), the velocity components in terms of Mach number and flow angles (M, α, β), and the body-axis components of the angular velocity vector (p,q,r). A stability-derivative aerodynamic model was used to model the aerodynamic loads needed for the aircraft equations of motion. The static and dynamic derivatives might be obtained from solution of indicial functions at relatively long time after the excitation of forcing parameters. For example, the lift coefficient can be obtained as:

$$C_L = C_{L0}(M) + C_{L\alpha}(t = \infty, \alpha, M)\alpha + C_{Lq}(t = \infty, M)q + C_{L\delta_p}\delta_p \tag{27}$$

where, $C_{L0}(M)$ is the trimmed lift coefficient at free-stream Mach number of M and $C_{L\delta_p}$ shows the pitch control increments in lift coefficient, where the control derivatives for the test case are obtained from the work of Vallespin et al.[52]

III. Test Case and Validation

A generic UCAV (Stability And Control CONfiguration, SACCON) shown in Fig. 2 is considered in this paper. The SACCON geometry and experimental data were provided to the partners participating in NATO RTO Task Group AVT-161 (Assessment of Stability and Control prediction Methods for NATO Air and Sea Vehicles).[53] The objective of this task group is to evaluate CFD codes against wind tunnel results. The vehicle planform and section profiles were defined in cooperation between the German Aerospace Center (DLR) and EADS-MAS. DLR adjusted the pre-design geometry for wind tunnel design purposes which actually led to a higher overall thickness at the root chord to provide enough space for the internal strain gauge balance. The aircraft has a lambda wing planform with a leading edge sweep angle of 53^o as shown in Fig. 2. The root chord is approximately 1 m, the wing span is 1.53 m, the reference chord is 0.48 m, and the reference area is 0.77 m^2. The main sections of the model are the fuselage, the wing section, and wing tip. The configuration is defined by three different profiles at the root section of the fuselage, two sections with the same profile at the inner wing, forming the transition from the fuselage to wing and the outer wing section. Finally, the outer wing section profile is twisted by 5^o around the leading edge to reduce the aerodynamic loads and shift the onset of flow separation to higher angles of attack.

The wind tunnel model was designed and manufactured at NASA Langley Research Center (LaRC). The model was designed to accommodate a belly sting mount for tests in the German-Dutch Low Speed Wing Tunnel (DNW-NWB) at DLR in Braunschweig and the $14' \times 22'$ low speed wind tunnel at NASA LaRC. Two meshes are available: the first uses a belly mounted sting present in the experiments and the second has no sting. The meshes were generated in two steps. In the first step, the inviscid tetrahedral mesh was generated using the ICEMCFD code. This mesh was then used as a background mesh by TRITET[54,55] which builds prism layers using an advancing front technique. TRITET rebuilds the inviscid mesh while respecting the size of the original inviscid mesh from ICEMCFD. These grids are shown in Fig. 3. and contain around 9M points and 26M cells. CFD simulations were run on the Cray XE6 (open system) machine at the Engineering Research Development Center (ERDC) [the machine name is Chugach with 2.3GHz core speed and 11,000 cores].

The coefficients of lift, drag, and pitch moment are compared with experiments in Fig. 3. This figure shows that the CFD predictions closely follow the trends of the experimental data up to moderate angles of attack. The offsets in the low angle of attack pitch moment in the model is likely due to the effects of the belly sting mounting present in the experiments.[56] Some of the SACCON aerodynamic features are shown in Fig. 4. Two emanating vortices from the wing tip and apex are present at 14^o angle of attack (Fig. 4(a)). These vortices lead to a negative pressure region on the upper wing surface and hence augment the lift force. As the angle of attack increases from 16^o, the onset point of the outboard vortex starts to travel toward the wing apex due to increasing adverse pressure gradients. At 19.5^o angle of attack, the vortices are already interacting as shown in Fig. 4(b). Further increasing of the angle of attack causes the inboard vortex to start to breakdown (Fig. 4(c)). At higher angles of attack the tip vortex also breaks down. The interaction of the vortices produces a strong recirculation zone over the upper wing (Fig. 4(d)) and results in wing stall and the aerodynamic center backward movement.

For CFD simulations of a maneuvering SACCON, the mesh without the sting geometry was used. Also for the generation of SACCON maneuvers, the wind tunnel model was scaled up to fit the characteristics of a full size aircraft if this were to fly. Initially, estimations of the mass and moments of inertia were made, through work carried out in the NATO group, based on the Northrop YB-46 aircraft. Table 1 summarizes the SACCON flyable geometry parameters and mass and inertia.

Table 1. Geometry parameters and Mass/Inertias of SACCON flyable model

Mean Aerodynamic Chord, $\bar{c}$ (m)	5.011
Wing Area, S (m^2)	55.0
Wing Span, b (m)	13.0
Ixx ($kg.m^2$)	8014
Iyy ($kg.m^2$)	6564
Izz ($kg.m^2$)	8937
Maximum take-off weight, MTWO (kg)	2000

IV. Results and Discussion

From the ROM equations given above, the unsteady aerodynamic responses to a wide range of aircraft maneuvers can be evaluated. These equations could predict the variations in the Mach number, angular rates, incidence, and side-slip angles during flight maneuvers. For SACCON maneuvers, the incidence and side-slip angles are in the range of -10 to 10 degrees with a maximum Mach number of 0.5. For surrogate modeling of indicial functions, a set of samples including 33 points is defined on the α and M space using factorial design. These points are uniformly spaced over α for Mach numbers of 0.1, 0.3, and 0.5 and are shown in Fig. 5. Also, it is assumed that the aerodynamic forces and moments are symmetric about zero degrees angle of attack and hence only the angles between zero and ten degrees are considered for response function calculations although this probably is not correct.

In the present paper, the response functions are directly calculated from unsteady RANS simulations and using a grid motion tool. All computations started from a steady-state solution and then advanced in time using second-order accuracy. The motion files were generated for step changes in aircraft forcing parameters (angle of attack, side-slip angle, and angular rates). These files define the rotations and displacements at discrete time instants and *Cobalt* then interpolates motion data using cubic-splines and moves the grid for each computational time step. The grid undergoes only translation motion for α and β responses, where the relative velocity between grid and flow at each instant defines the angle of attack and side-slip. For angular rate responses, the grid rotates and translates simultaneously. Again, a translation motion was used in order to keep angles of attack and side-slip zero during rotations.

The indicial functions with respect to the angle of attack are calculated using the CFD and grid motion approach for each sample conditions. In these simulations, the solution starts from a steady-state condition with zero degrees angle of attack at a Mach number of M_i, and then iterates such that angle of attack is held constant at α_i for all $t > 0$, where M_i and α_i correspond to samples shown in Fig 5, excluding the samples at zero degrees angle. In these calculations, the side-slip angle is zero degrees at all times and the grid does not rotate at any time. The lift and pitch moment indicial responses to a unit step change in the angle of attack, i.e. $\alpha_i = 1$, are shown in Figs. 6(a) and (b) for Mach numbers of 0.1, 0.3, and 0.5. The lift and pitch moment are plotted against the nondimensional time $s = 2Vt/c$, where V is the frees-stream velocity, t is the response time, and c is the reference length. Figure 6(a) shows that the lift responses have a peak at $s = 0$. Likewise, the pitch moment predicts a negative peak at this time as shown in Fig. 6(b). As the steady flow around the vehicle is disturbed by the grid motion, a compression wave and an expansion wave are formed on the lower and upper surface of the vehicle that cause a sharp peak in the responses.[25] As the response time progresses, the waves begin to move away from the vehicle and the lift and pitch moment responses start to increase and then asymptotically reach the steady-state values. Figures 6(a) and (b) also show that the initial peak becomes smaller for compressible flow. An explanation is given by Leishman;[57] this is due to the propagation of pressure disturbances at the speed of sound, compared to the incompressible case, where the disturbances propagate at infinite speed.

The nonlinear indicial functions are generated using the response functions at different angle of attack intervals. For example, to determine $C_{L\alpha}(t, \alpha)$ and $C_{m\alpha}(t, \alpha)$ terms, the lift and pitch moment responses to the angles of α_{i-1} and α_i, are estimated using a surrogate model from available samples. These two angles can be chosen by the user, but $\alpha_{i-1} < \alpha \leq \alpha_i$ should apply. The difference between these responses divided by the interval length, i.e. $\alpha_i - \alpha_{i-1}$, results in the indicial functions at the interval. Figures 6(c) and (d) show the interval lift and pitch moment responses at different angles of attack at Mach number of 0.3. These figures show that the initial values of responses are invariant with angle of attack, but the transient trend and steady state values change depending on the angle of attack. The changes in the indicial functions are nearly small since the lift and pitch moment are in nearly linear regime of angle of attack.

The lateral loads response to a unit step change in the side-slip angle at different angles of attack are shown in Fig. 7 for Mach number of 0.1, 0.3, and 0.5. In these simulations, the solution starts from a steady-state condition at zero degrees side-slip angle and an angle of attack of α_i at a Mach number of M_i, and then iterates such that the side-slip angle is held constant to one degree and angle of attack is held constant to α_i for all $t > 0$, where M_i and α_i correspond to the samples shown in Fig. 5. Likewise, for the lift and pitch moment, the initial peaks in lateral responses become smaller for compressible flow. Figure 7 shows that side-force responses ($C_{y\beta}$) remain almost unchanged with the changes in the angle of attack for the range of angles studied. This figure shows that the yaw moment responses ($C_{n\beta}$) slightly change with the changes in the angle of attack, but significant differences are found for the roll moment. The differences become more apparent as Mach number increases.

Typically, the angle of attack effects are negligible for the responses due to the angular rates at low to moderate angles of attacks. Figures 8(a)-(b) show the lift and pitch moment responses respectively with a unit step change in pitch rate for Mach numbers of 0.1, 0.3, and 0.5. Again there is an initial jump in lift as grid starts to rotate which its value decreases as Mach number increases. The lift response starts to fall a short time after initial excitation and then it reaches asymptotically a steady-state value, the so called pitch dynamic derivative. Figures 8(a)-(b) show that increasing Mach number results in the slight decrease of the lift and pitch damping derivatives. These calculations, along with a time-dependent surrogate model, were used to estimate the functions of $C_{Lq}(t, M)$ and $C_{mq}(t, M)$ in the ROM equations. Also, the indicial functions with respect to roll and yaw rates are shown in Figs. 9-10, respectively. These calculations, along with a time-dependent surrogate model, were used to estimate the functions of $C_{Yp}(t, M)$, $C_{lp}(t, M)$, $C_{np}(t, M)$, $C_{Yr}(t, M)$, $C_{lr}(t, M)$, and $C_{nr}(t, M)$ in the ROM equations.

The ROM equations were used for prediction of two SACCON maneuvers: a half Lazy-8[58] and an Immelmann turn.[59] In both maneuvers, the aircraft enters and terminates the maneuver from a straight and level condition. The maneuvers were generated using DIDO to minimize final maneuver time subject to vehicle aerodynamics, mass properties, state and control constraints. The angle of attack and side-slip angles are limited to $[-10^o, 10^o]$ while the maximum Mach number is 0.5. Figure 11 shows that the Lazy-8 maneuver makes a 180^o degree turn. The airplane starts a climb steeply to reduce flight speed as shown in Fig.11-(b). This reduced speed helps to have a smaller radius turn and total traveled time.[59] Next, the airplane starts to roll as the pitch angle decreases, where at 90^o yaw angle, the vehicle is at zero pitch and maximum roll angle as shown in Fig.11-(d). This is followed by a descent trajectory and decreasing of roll angle, increasing pitch angle, and regaining the speed until the vehicle reaches initial velocity and altitude. The Immelmann turn as shown in Fig. 12 comprises a half loop with a half roll at the end. The maneuver starts with a steep climb and thus decreases the speed as shown in Fig. 12-(b). At the maximum pitch angle, the aircraft heading suddenly changes from 0^o to 180^o, which makes the aircraft final flight path exactly opposite of the initial path. As the heading starts to increase, the aircraft performs a half roll to level the wing as shown in Fig. 12-(d). The final altitude is slightly higher than starting altitude as shown in Fig. 12-(a).

Figure 13 depicts the predicted aerodynamic loads of half Lazy-8 maneuver. The comparisons between the created ROM with the full-order model shows good agreements in all coefficients. The predictions of aerodynamic loads for the Immelmann turn are also shown in Fig. 14. Again, the ROM is in close agreement with the full-order model for all coefficients. Note that the cost of generating each full-order model is approximately 192 wall-clock hours using 256 processors (2.3 GHz), but the model predictions are generated within a few seconds. Finally, the surface pressure distributions during maneuvers are shown in Fig. 15. The leading edge vortex can be seen behind the leading edge on the upper wing around ten degrees angle of attack during the maneuvers.

V. Conclusions

This paper investigates the use of ROMs that significantly reduce the CFD simulation time required to create a full aerodynamics database, making it possible to accurately model aircraft static and dynamic characteristics from a limited number of time-accurate CFD simulations. The ROM considered was based on Duhamel's superposition integral using indicial (step) response functions. The indical functions consist of aircraft responses to step changes in the angle of attack, pitch rate, side-slip angle, roll, and yaw rates. All these functions were calculated using direct response simulation in URANS with the aid of rigid grid motion tool. A time-dependent surrogate model was described to find the response functions dependency on the angles of attack and Mach numbers.

The test case used was the SACCON UCAV scaled up to fit the characteristics of a full size. Two time-optimal maneuvers were generated using DIDO code to minimize final maneuver time subject to vehicle aerodynamics, mass properties, state and control constraints. The comparison between unsteady simulation of maneuvers with ROM predictions showed the consistency of predictions for all coefficients. The cost of generating each full-order model was approximately 192 wall-clock hours, but the model predictions were generated in a few seconds. The results give us confidence in the ability of response type CFD calculations for aerodynamic loads modeling and hence to extend out this method for fast-rate maneuvers.

VI. Acknowledgements

Mehdi Ghoreyshi was supported by the National Research Council/US Air Force Office of Scientific Research. Their financial support is gratefully acknowledged. Acknowledgements are expressed to the Department of Defense Engineering Research Development Center (ERDC) for providing computer time. The SACCON geometry was provided by NATO RTO Task Group AVT-161 on Assessment of Stability and Control Prediction Methods for NATO Air & Sea Vehicles. The authors appreciate the support provided by the Modeling and Simulation Research Center at USAFA.

References

[1]Pamadi, B. N., *Performance, Stability, Dynamics, and Control of Airplanes*, AIAA Education Series, Second Edition, Reston, VA, USA, 2004.

[2]Chambers, J. R. and Hall, R. M., "Historical Review of Uncommanded Lateral-Directional Motions at Transonic Conditions," *Journal of Aircraft*, Vol. 41, No. 3, 2004, pp. 436–447.

[3]Hall, R. M., Woodson, S. H., and Chambers, J. R., "Accomplishments of the Abrupt-Wing-Stall Program," *Journal of Aircraft*, Vol. 42, No. 3, 2005, pp. 653–660.

[4]Hall, R. M., "Overview of the Abrupt Wing Stall Program," *Progress in Aerospace Sciences*, Vol. 40, No. 7, 2004, pp. 417–452.

[5]Liebe, R., *Flow Phenomena in Nature: A Challenge to Engineering Design*, WIT Press, Southampton, Great Britain, 2007.

[6]Schütte, A., Einarsson, G., Raichle, A., Schoning, B., Mönnich, W., and Forkert, T., "Numerical Simulation of Manoeuvreing Aircraft by Aerodynamic, Flight Mechanics, and Structural Mechanics Coupling," *Journal of Aircraft*, Vol. 46, No. 1, 2009, pp. 53–64.

[7]Ghoreyshi, M., Jirásek, A., and Cummings, R. M., "CFD Modeling for Trajectory Predictions of a Generic Fighter Configuration," AIAA Paper 2011–6523, August 2011.

[8]Tobak, M. and Schiff, L. B., "On the Formulation of the Aerodynamic Characteristics in Aircraft Dynamics," NASA TR R–456, 1976.

[9]Murman, S. M., Chaderjian, N. M., and Pandya, S. A., "Automation of a Navier-Stokes S&C Database Generation for the Harrier in Ground Effect," AIAA Paper 2002–259, January 2002.

[10]Lisandrin, P., Carpentieri, G., and van Tooren, M., "Investigation over CFD-based Models for the Identification of Nonlinear Unsteady Aerodyanmics Responses," *AIAA Journal*, Vol. 44, No. 9, 2006, pp. 2043–2050.

[11]McDaniel, D. R., Cummings, R. M., Bergeron, K., Morton, S. A., and Dean, J. P., "Comparisons of CFD Solutions of Static and Maneuvering Fighter Aircraft with Flight Test Data," *Journal of Aerospace Engineering*, Vol. 223, No. 4, 2009, pp. 323–340.

[12]Cummings, R. M., Jirásek, A., Ghoreyshi, M., and Post, M. L., "Numerical Prediction of Stability Derivatives with Various Reduced Order Models," AVT-189 Specialists Meeting On Assessment of Stability and Control Prediction Methods for NATO Air and Sea Vehicles, Portsmouth, England, October 2011.

[13]Lucia, D. J., Beran, P. S., and Silva, W. A., "Reduced-Order Modeling: New Approaches For Computational Physics," *Progress in Aerospace Sciences*, Vol. 40, 2004, pp. 51–117.

[14]Jategaonkar, R. V., *Flight Vehicle System Identification*, 2006, AIAA Educational Series, Vol. 216, Reston, VA, USA.

[15]Ballhaus, W. F. and Goorjian, P. M., "Computation of Unsteady Transonic Flow by the Indicial Method," *AIAA Journal*, Vol. 16, No. 2, 1978, pp. 117–124.

[16]Tobak, M., Chapman, G. T., and Schiff, L. B., "Mathematical Modeling of the Aerodynamic Characteristics in Flight Dynamics," NASA TN–85880, 1984.

[17]Tobak, M. and Chapman, G. T., "Nonlinear Problems in Flight Dynamics Involving Aerodynamic Bifurcations," NASA TN–86706, 1985.

[18]Hall, K. C., Thomas, J. P., and Dowell, E. H., "Reduced-order Modelling of Unsteady Small-Disturbance Using a Frequency-Domain Proper Orthogonal Decomposition Technique," AIAA Paper 1999–655, January 1999.

[19]Gaitonde, A. and Jones, D. P., "Reduced Order State-Space Models from the Pulse Responses of a Linearized CFD Scheme," *International Journal of Numerical Methods in Fluids*, Vol. 42, No. 6, 2003, pp. 581–606.

[20]Silva, W. A. and Bartels, R. E., "Development of Reduced-Order Models for Aeroelastic Analysis and Flutter Prediction Using the CFL3Dv6.0 Code," *Journal of Fluids and Structures*, Vol. 19, No. 6, 2004, pp. 729–745.

[21]Jirásek, A., Jeans, T. L., Martenson, M., Cummings, R. M., and Bergeron, K., "Improved Methodologies For Maneuver Design of Aircraft Stability and Control Simulations," AIAA Paper 2010–515, January 2010.

[22]Goman, M. G. and Khrabov, A. N., "State-Space Representation of Aerodynamic Characteristics of An Aircraft at High Angles of Attack," AIAA Paper 92–4651, August 1992.

[23]Leishman, J. G. and Nguyen, K. Q., "State-Space Representation of Unsteady Airfoil Behavior," *AIAA Journal*, Vol. 28, No. 5, 1989, pp. 836–844.

[24]Manglano-Villamarine, C. E. and Shaw, S. T., "Three-dimensional Indicial Response of Finite Aspect Ratio Yawed Wings," *The Aeronautical Journal*, Vol. 111, No. 1120, 2007, pp. 359–371.

[25]Ghoryeshi, M., Jirásek, A., and Cummings, R. M., "Computational Investigation into the Use of Response Functions for Aerodynamic Loads Modeling," *AIAA Journal*, Vol. 50, No. 6, 2012, pp. 1314–1327.

[26]Manglano-Villamarine, C. E. and Shaw, S., "Three-dimensional Indicial Response of Finite Aspect Ratio Yawed Wing," *The Aeronautical Journal*, Vol. 111, No. 1120, 2007, pp. 359–371.

[27]Singh, R. and Baeder, J., "Direct Calculation of Three-Dimensional Indicial Lift Response Using Computational Fluid Dynamics," *Journal of Aircraft*, Vol. 34, No. 4, 1997, pp. 465–471.

[28]Raveh, D. E., "Reduced-Order Models for Nonlinear Unsteady Aerodynamics," *AIAA Journal*, Vol. 39, No. 8, 2001, pp. 1417–1429.

[29]Ghoreyshi, M. and Cummings, R. M., "Aerodynamics Modeling of a Maneuvering Aircraft Using Indicial Functions," AIAA Paper 2012–689, January 2012.

[30]Ghoreyshi, M., Badcock, K. J., and Woodgate, M. A., "Accelerating the Numerical Generation of Aerodynamic Models for Flight Simulation," *Journal of Aircraft*, Vol. 46, No. 3, 2009, pp. 972–980.

[31]Strang, W. Z., Tomaro, R. F., and Grismer, M. J., "The Defining Methods of Cobalt: A Parallel, Implicit, Unstructured Euler/Navier-Stokes Flow Solver," AIAA Paper 1999–0786, 1999.

[32]Da Ronch, A., Vallespin, D., Ghoreyshi, M., and Badcock, K. J., "Computation of Dynamic Derivatives Using CFD," AIAA Paper 2010–4817, June-July 2010.

[33]Gottlieb, J. J. and Groth, C. P. T., "Assessment of Riemann Solvers For Unsteady One-dimensional Inviscid Flows of Perfect Gasses," *Journal of Fluids and Structure*, Vol. 78, No. 2, 1998, pp. 437–458.

[34]Tomaro, R. F., Strang, W. Z., and Sankar, L. N., "An Implicit Algorithm For Solving Time Dependent Flows on Unstructured Grids," AIAA Paper 1997–0333, January, 1997.

[35]Forsythe, J. R., Hoffmann, K. A., Cummings, R. M., and Squires, K. D., "Detached-Eddy Simulation With Compressibility Corrections Applied to a Supersonic Axisymmetric Base," *Journal of Fluids Engineering*, Vol. 124, No. 4, 2002, pp. 911–923.

[36]Forsythe, J. R. and Woodson, S. H., "Unsteady Computations of Abrupt Wing Stall Using Detached-Eddy Simulations," *Journal of Aircraft*, Vol. 42, No. 3, 2005, pp. 606–616.

[37]Morton, S. A., Forsythe, J. R., Mitchell, A. M., and Hajek, D., "Detached-Eddy Simulations and Reynolds-Averaged Navier-Stokes Simulations of Delta Wing Vortical Flowfields," *Journal of Fluids Engineering*, Vol. 124, No. 4, 2002, pp. 924–932.

[38]Forsythe, R., Squires, K. D., Wurtzler, K. E., and Spalart, P. R., "Detached-Eddy Simulation of Fighter Aircraft at High Alpha," *Journal of Aircraft*, Vol. 41, No. 2, 2004, pp. 193–200.

[39]Jeans, T., McDaniel, D., Cummings, R. M., and Mason, W., "Aerodynamic Analysis of a Generic Fighter Using Delayed Detached-Eddy Simulations," *Journal of Aircraft*, Vol. 46, No. 4, 2009, pp. 1326–1339.

[40]Romero, D. A., Amon, C., Finger, S., and Verdinelli, I., "Multi-Stage Bayesian Surrogates For the Design of Time-Dependent System," *Proceedings of ASME 2004 Design Engineering Technical Conference and Computers and Information in Engineering*, DETC 2004-57510, 2004.

[41]Jones, D. R., Schonlau, M., and Welch, W. J., "Efficient Global Optimization of Expensive Black-Box Functions," *Kluwer Academic Publishers*, Vol. 13, 1998, pp. 455–492.

[42]Wagner, H., "Über die Entstehung des Dynamischen Auftriebes von Tragflügeln," *Zeitschrift für Angewandte Mathematik und Mechanik*, Vol. 1, 1925, pp. 17–35.

[43]Leishman, J. G., "Subsonic Unsteady Aerodynamics Caused by Gusts Using the Indicial Method," *Journal of Aircraft*, Vol. 33, No. 5, 1996, pp. 869–879.

[44]Lomax, H., "Indicial Aerodynamics," AGARD Manual of Aeroelasticity, Part II, Chapter 6, 1960.

[45]Betts, J. T., "Survey of Numerical Methods for Trajectory Optimization," *Journal of Guidance, Control, and Dynamics*, Vol. 20, No. 1, 1997, pp. 57–60.

[46]Hull, D. G., "Conversion of Optimal Control Problems into Parameter Optimization Problems," *Journal of Guidance, Control, and Dynamics*, Vol. 21, No. 2, 1998, pp. 193–207.

[47]Brinkman, K. and Visser, H. G., "Optimal Turn-Back Maneuvre After Engine Failure in a Single-Engine Aircraft During Climb-Out," *Journal of Aerospace Engineering*, Vol. 22, No. G, 2006, pp. 17–27.

[48]Ross, I. M. and Fahroo, F., "User's Manual for DIDO 2002: A MATLAB Application Package for Dynamic Optimization," NPS Technical Rept, Dept. of Aeronautics and Astronautics, Naval Postgraduate School, AA-02-002, 2002.

[49]Canuto, C., Hussaini, M. Y., Quarteroni, A., and Zang, T. A., *Spectral Methods in Fluid Dynamics*, Springer-Verlag, New York, 1988.

[50]Kazemi, M. A. and Razzaghi, M., "The Pseudospectral Legendre Method for Discretizing Optimal Control Problems," *IEEE Transactions on Automatic Control*, Vol. 40, No. 10, 1995, pp. 1793–1796.

[51]Etkin, B., *Dynamics of Atmospheric Flight*, Dover Publications, New York, 2000.

[52]Vallespin, D., Ghoreyshi, M., and Badcock, K. J., "Assessment of the Limits of Tabular Aerodynamic Models for Flight Dynamics Analysis Using the SACCON UCAV Configuration," RAes Aerodynamic Conference, University of Bristol, July 201.

[53]Cummings, R. M. and Schütte, A., "An Integrated Computational/Experimental Approach to UCAV Stability & Control Estimation: Overview of NATO RTO AVT-161," AIAA Paper 2010–4392, June-July 2010.

[54]Tyssel, L., "Hybrid Grid Generation for Complex 3D Geometries," Proceedings of the 7th International Conference on Numerical Grid Generation in Computational Field Simulation, 2000, pp. 337–346.

[55]Tyssel, L., "The TRITET Grid Generation System," International Society of Grid Generation (ISGG)," Proceedings of the 10th International Conference on Numerical Grid Generation in Computational Field Simulations, Forth, Crete, Greece, 2000.

[56]Jirásek, A. and Cummings, R. M., "SACCON Static and Dynamic Motion Flow Physics Simulations Using COBALT," AIAA Paper 2011-3965, June 2011.

[57]Leishman, J. G., "Indicial Lift Approximations for Two-Dimensional Subsonic Flow as Obtained from Oscillatory Measurements," *Journal of Aircraft*, Vol. 30, No. 3, 1993, pp. 340–351.

[58]Love, M. C., *Flight Maneuvers*, McGraw-Hill, New York, USA, 1999.

[59]Anderson, F., *Flying the Mountains: A Training Manual for Flying Single-Engine Aircraft*, McGraw-Hill, New York, USA, 2003.

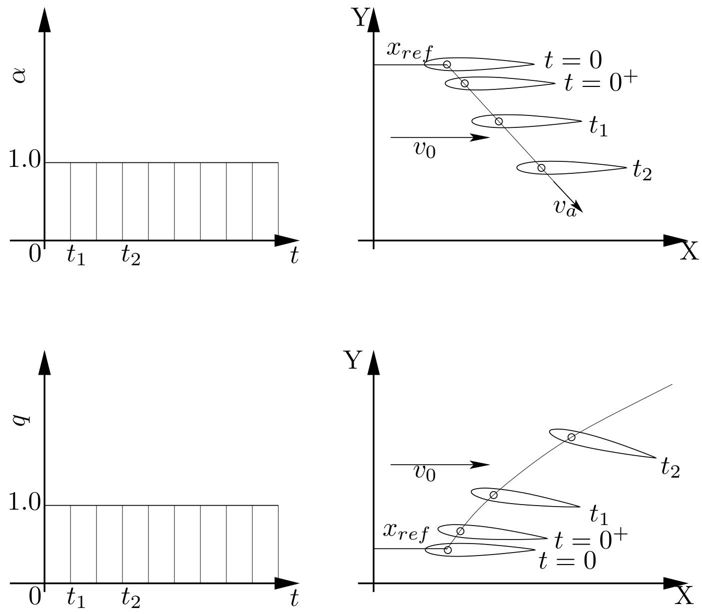

Figure 1. The grid motion for modeling a step change in angle of attack and pitch rate.

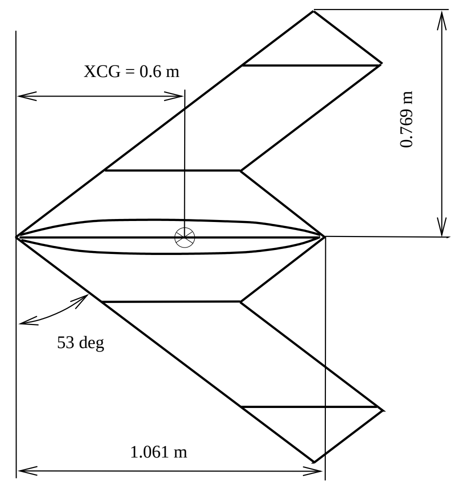

Figure 2. UCAV SACCON geometry.

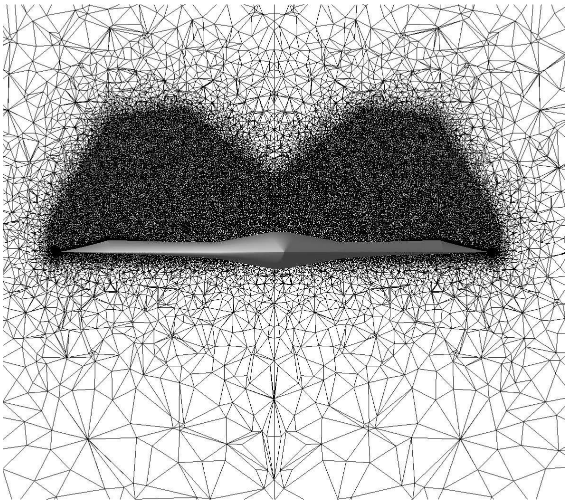

(a) grid without sting geometry.

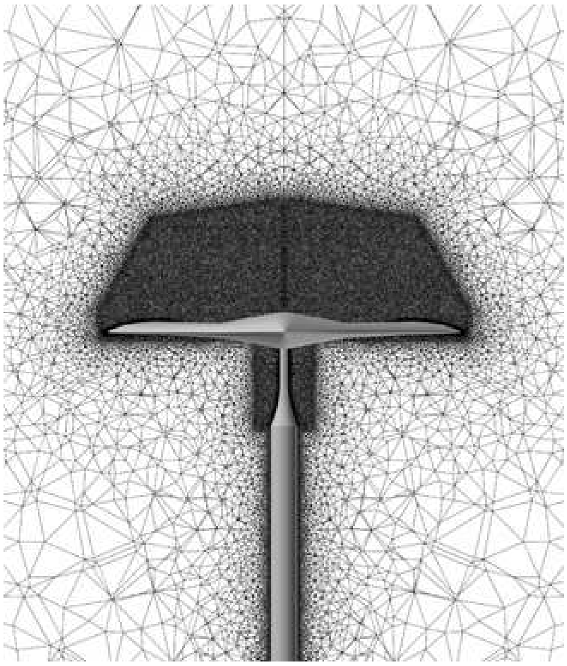

(b) grid with sting geometry.

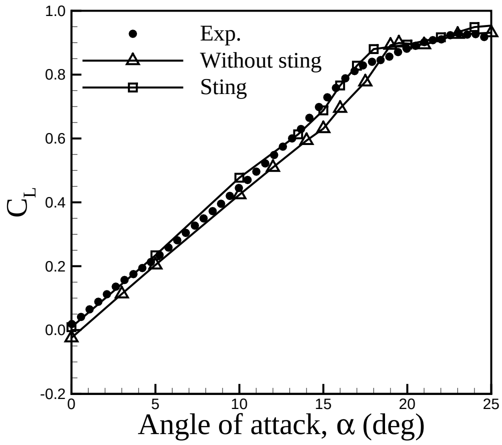

(c) Static lift coefficient

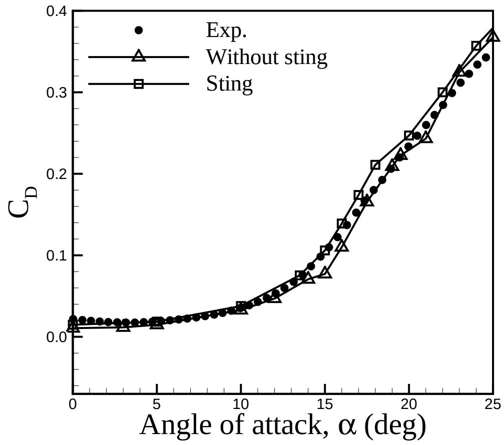

(d) Static drag coefficient

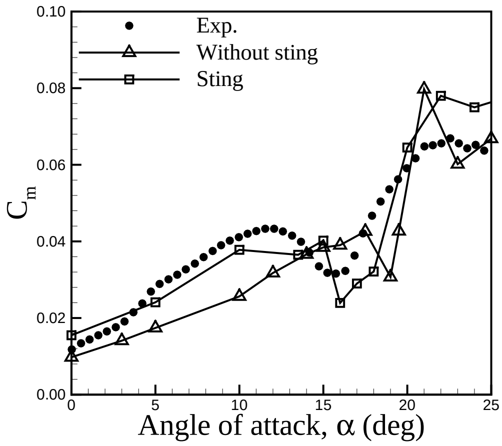

(d) Static pitch moment coefficient

Figure 3. The SACCON grids and static predictions at M_∞=0.144 and $Re = 1.61 \times 10^6$.

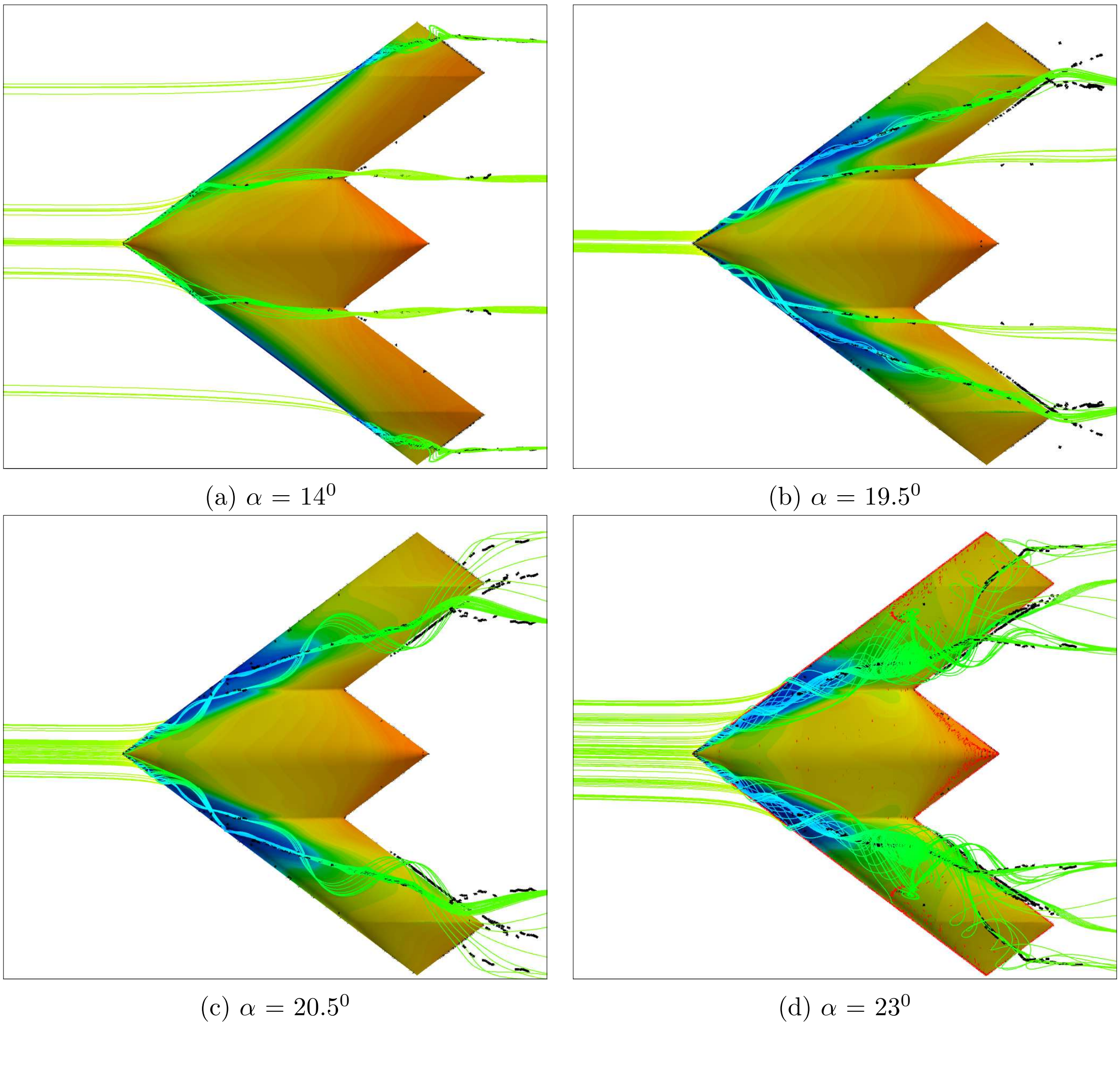

(a) $\alpha = 14^0$ (b) $\alpha = 19.5^0$

(c) $\alpha = 20.5^0$ (d) $\alpha = 23^0$

Figure 4. The SACCON vortical flows using SA turbulence model. The conditions are : M_∞=0.144 and $Re = 1.61 \times 10^6$. The vortices core lines are extracted and shown by black lines. For case (d), the flow separations lines are shown by red lines.

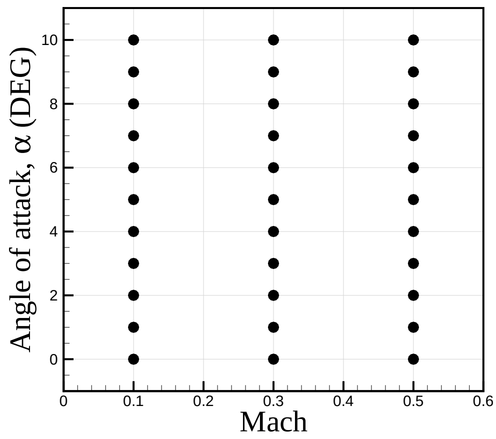

Figure 5. Design space samples.

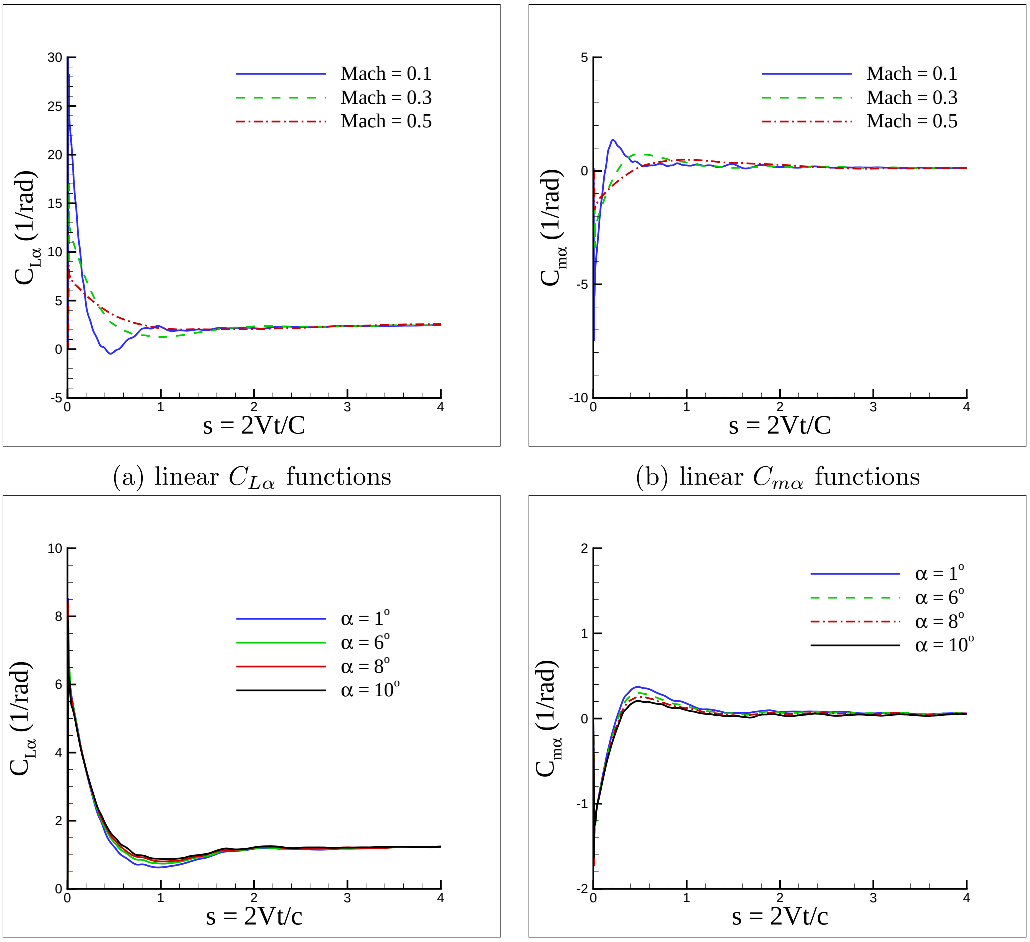

(a) linear $C_{L\alpha}$ functions (b) linear $C_{m\alpha}$ functions

(c) nonlinear $C_{L\alpha}$ functions at M=0.3 (d) nonlinear $C_{m\alpha}$ functions at M=0.3

Figure 6. The lift and pitch moment indicial functions.

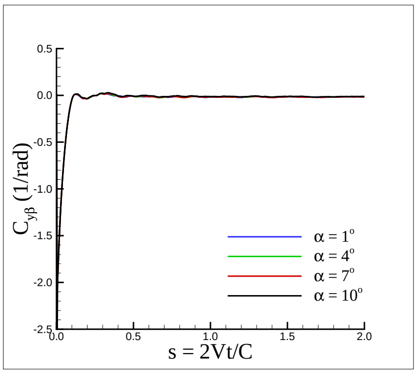

(a) $C_{Y\beta}$ functions at M =0.1

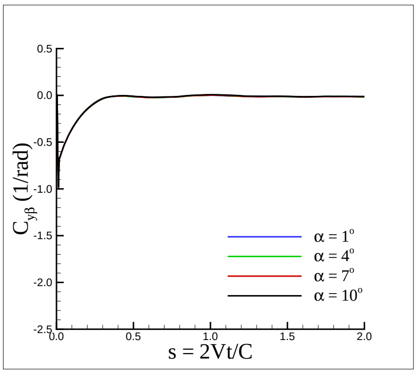

(b) $C_{Y\beta}$ functions at M =0.3

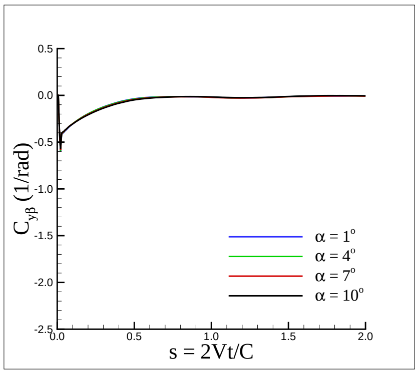

(c) $C_{Y\beta}$ functions at M =0.5

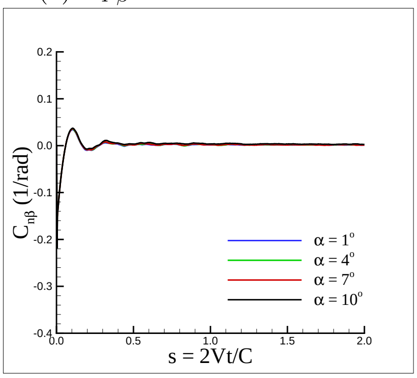

(d) $C_{n\beta}$ functions at M =0.1

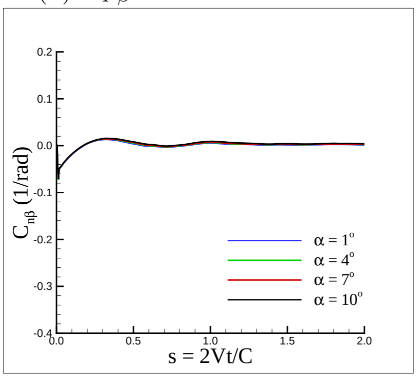

(e) $C_{n\beta}$ functions at M =0.3

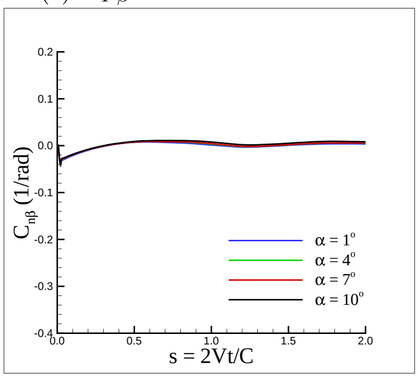

(f) $C_{n\beta}$ functions at M =0.5

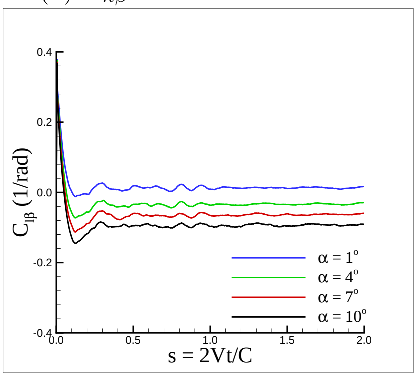

(g) $C_{l\beta}$ functions at M =0.1

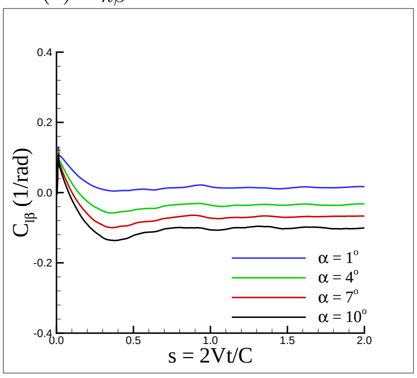

(h) $C_{l\beta}$ functions at M =0.3

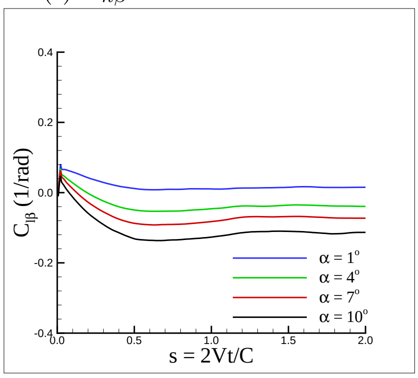

(i) $C_{l\beta}$ functions at M =0.5

Figure 7. The side-force, roll and yaw moments indicial functions.

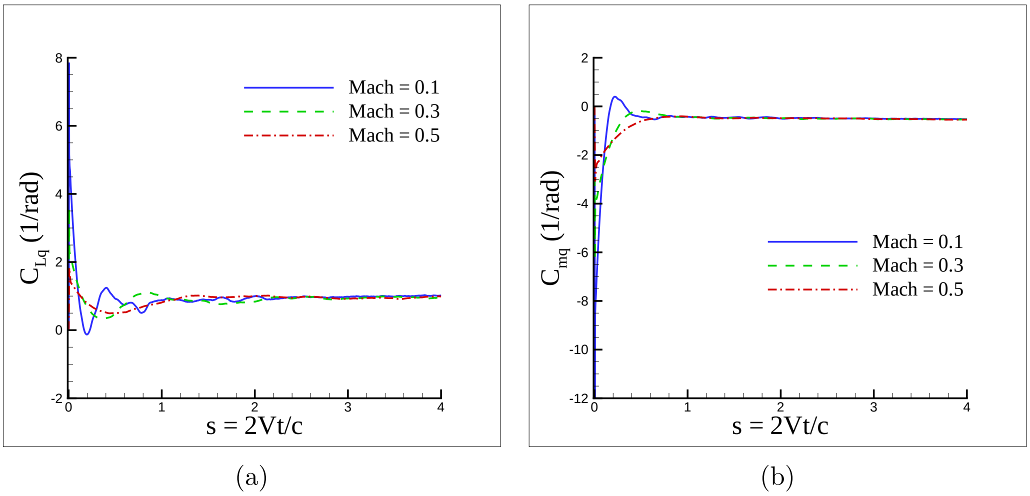

Figure 8. The lift and pitch moment indicial functions with a unit step change of normalized pitch rate at different Mach numbers.

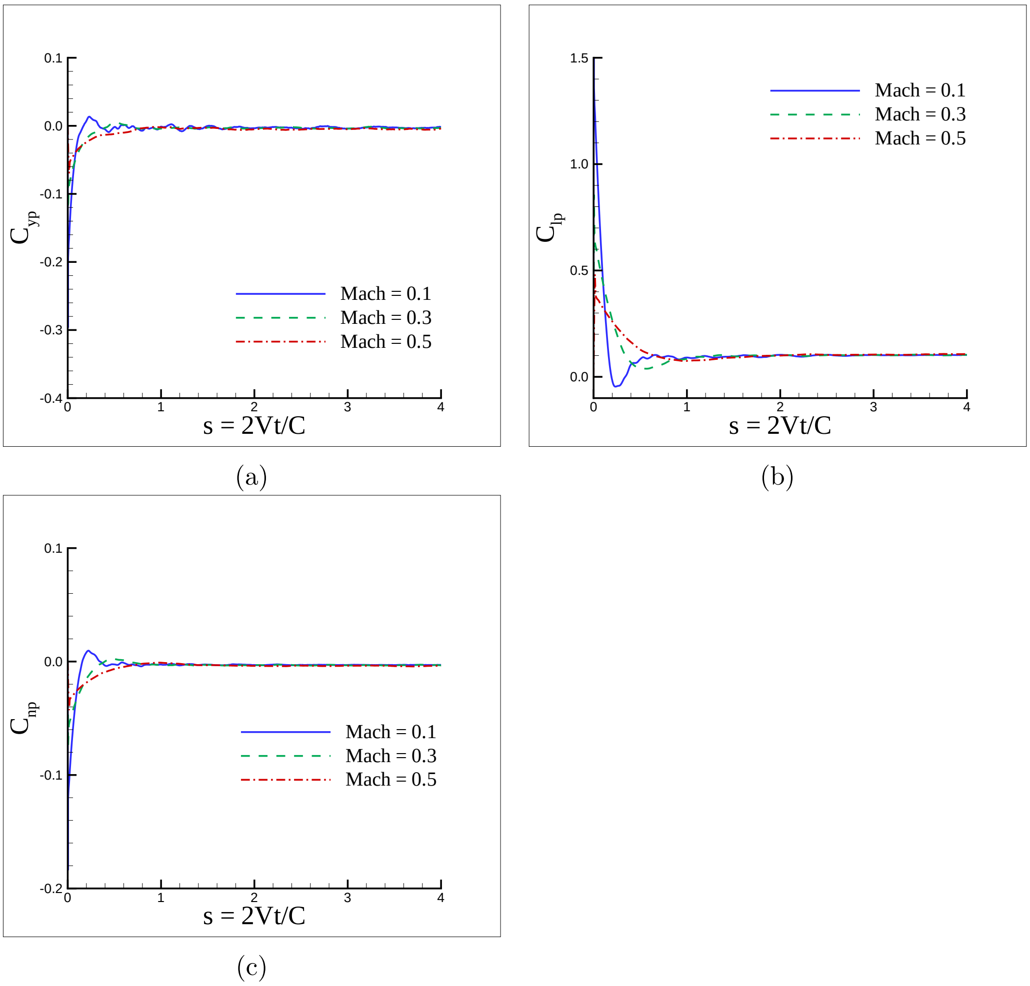

Figure 9. The lateral coefficients with a unit step change in the normalized roll rate.

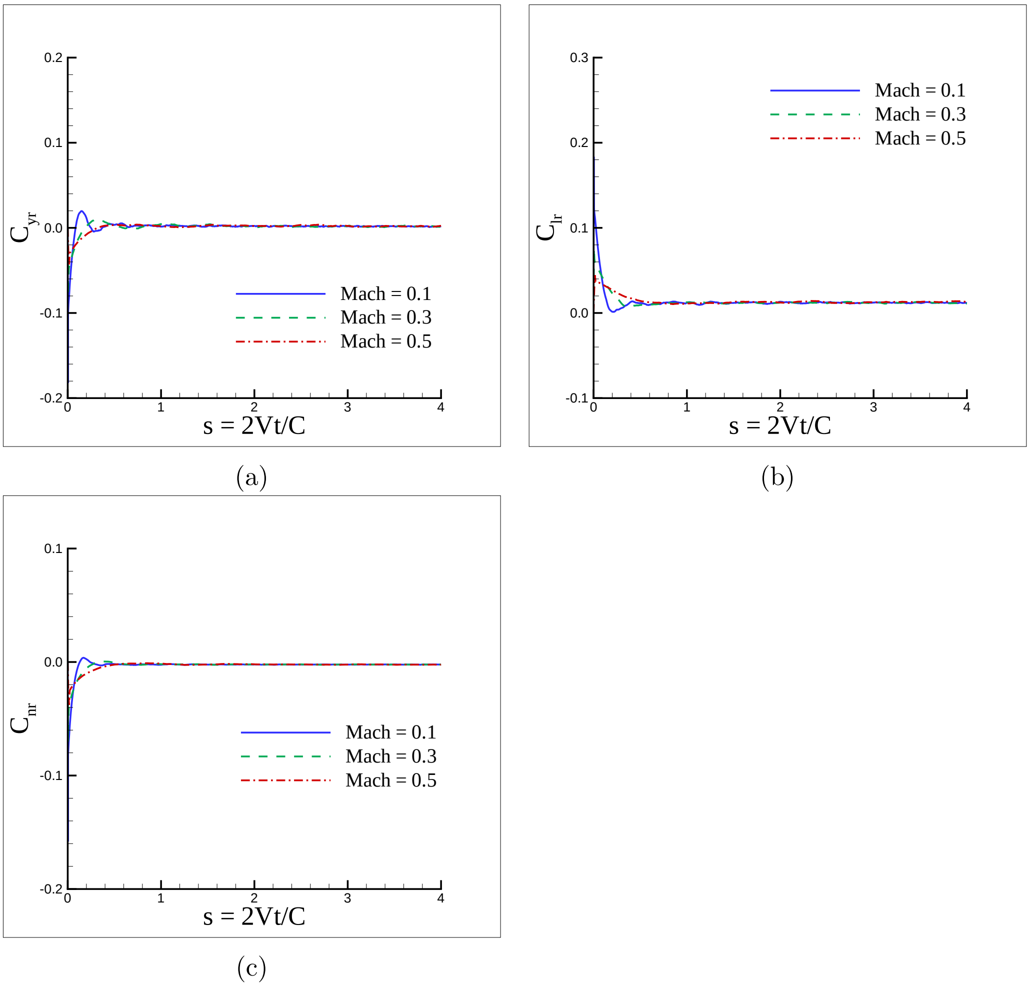

Figure 10. The lateral coefficients with a unit step change in the normalized yaw rate.

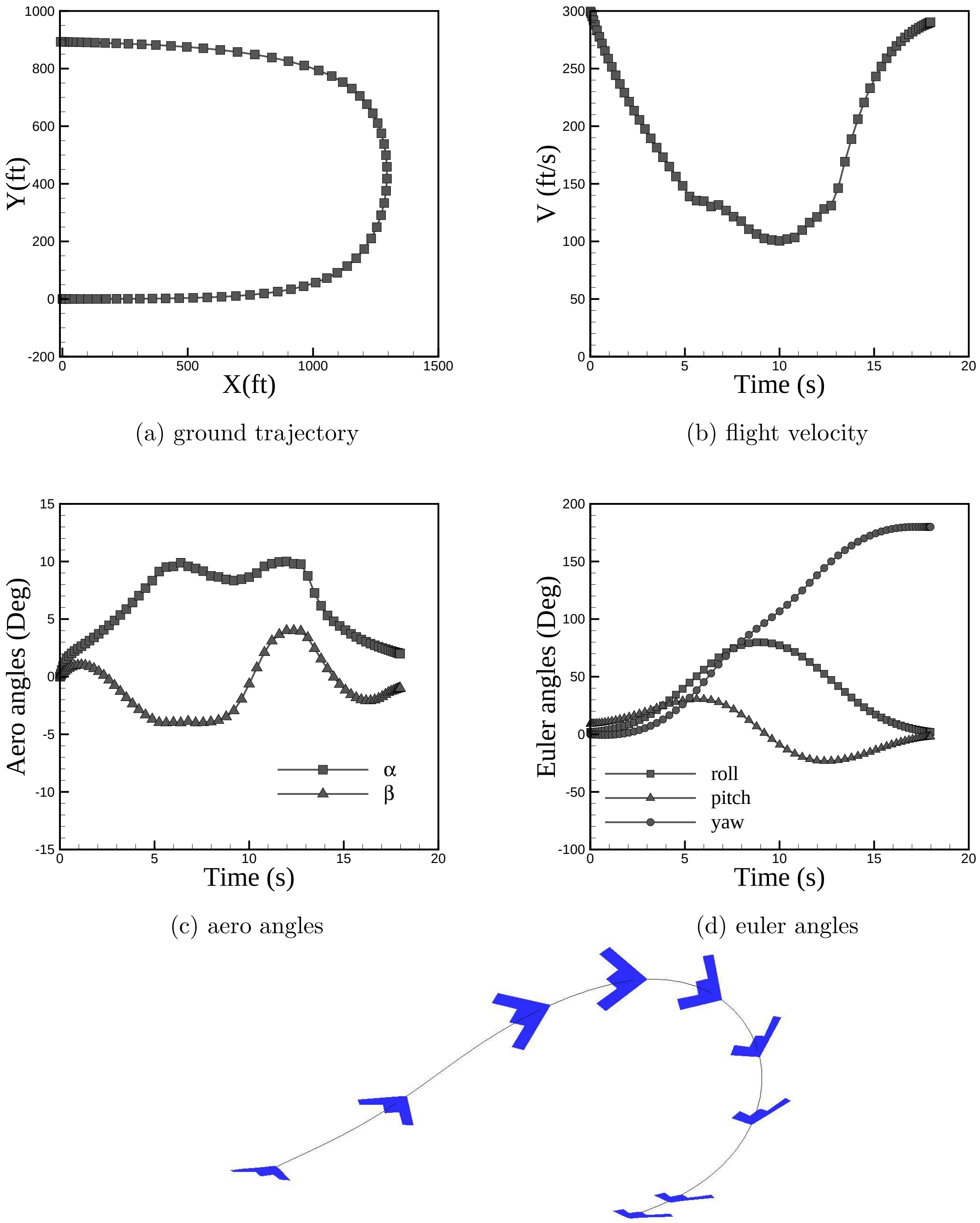

(a) ground trajectory
(b) flight velocity
(c) aero angles
(d) euler angles
(e) Flight trajectory

Figure 11. Half lazy-8 maneuver.

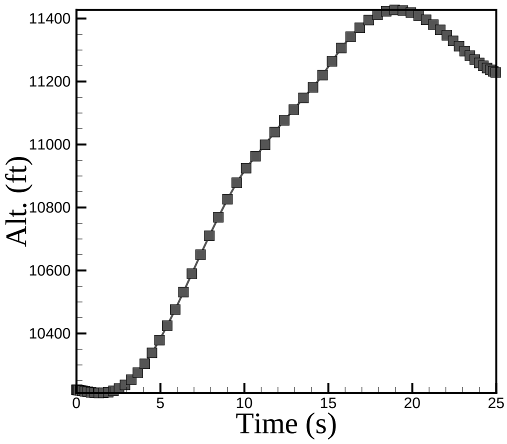

(a) flight altitude

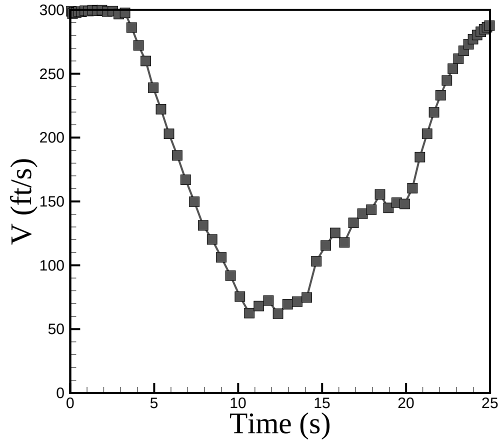

(b) flight velocity

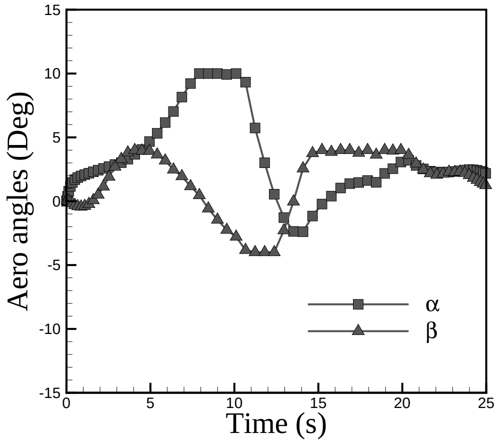

(c) aero angles

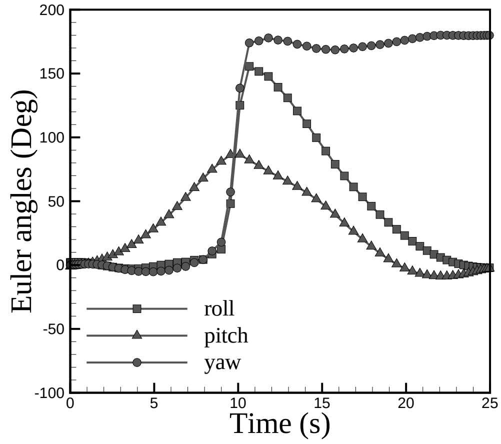

(d) euler angles

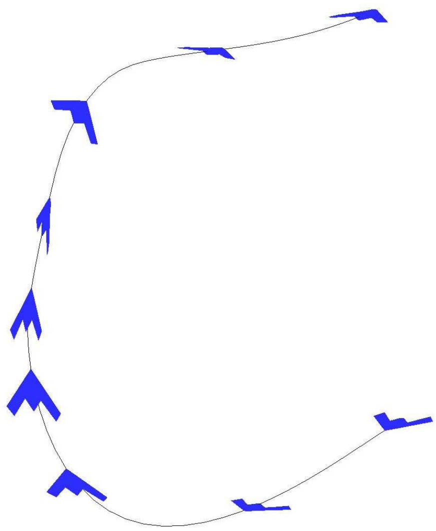

(e) Flight trajectory

Figure 12. Immelmann turn maneuver.

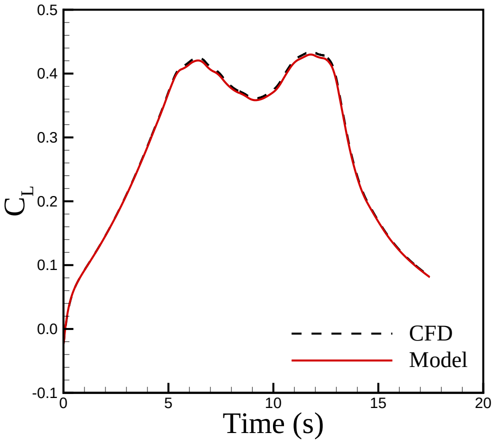

(a) Lift coefficient

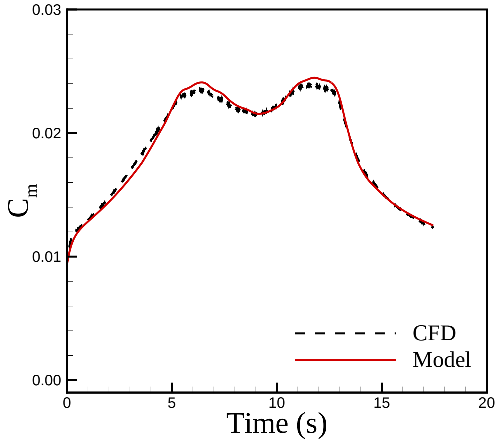

(b) Pitch moment coefficient

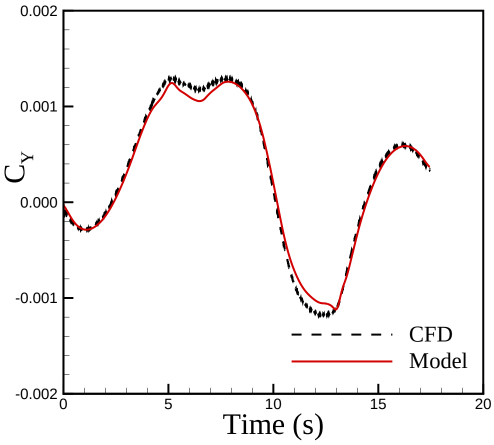

(c) Side-force coefficient

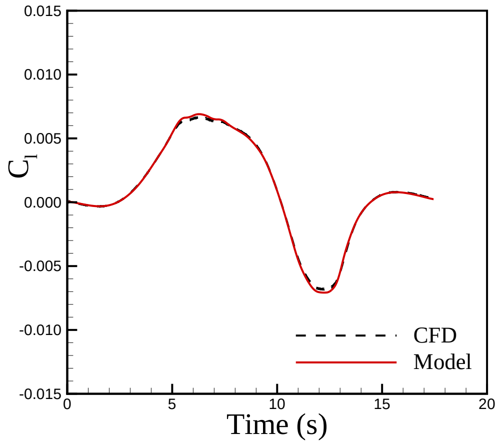

(d) Roll moment coefficient

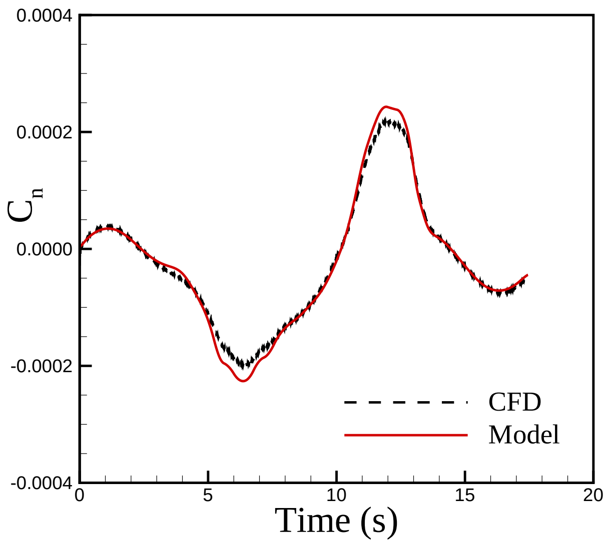

(e) Yaw moment coefficient

Figure 13. Aerodynamic modeling of half lazy-8 maneuver.

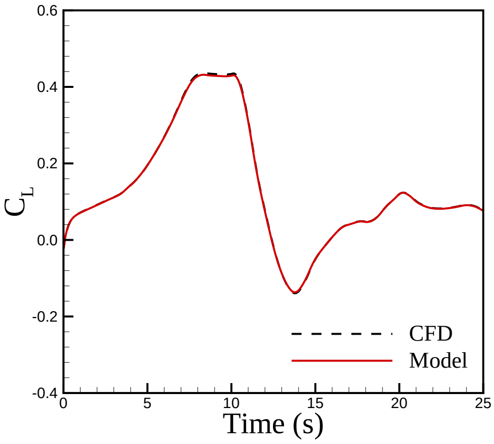

(a) Lift coefficient

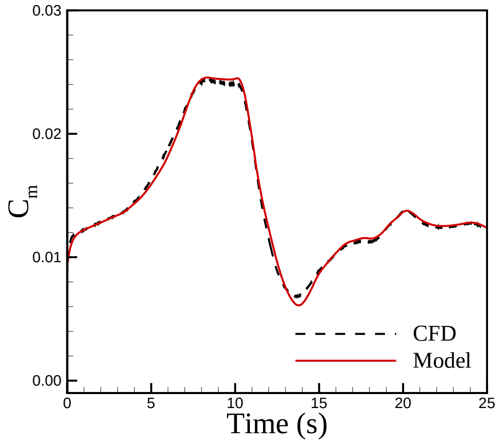

(b) Pitch moment coefficient

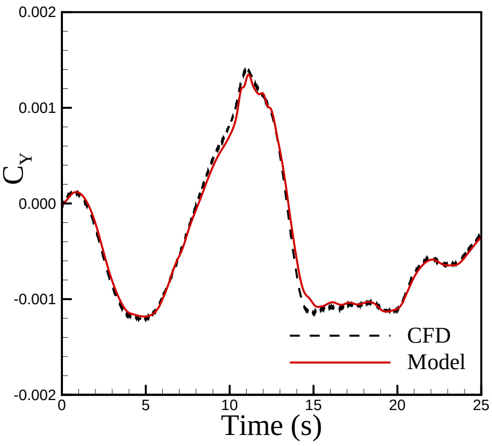

(c) Side-force coefficient

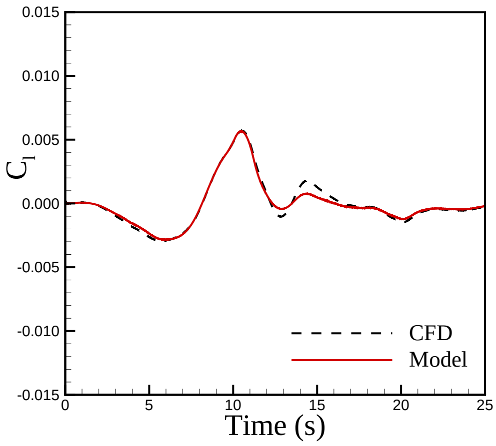

(d) Roll moment coefficient

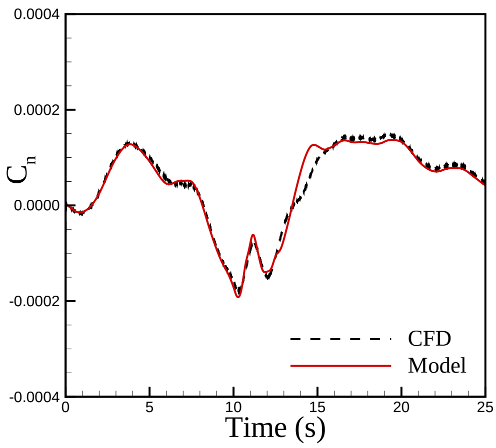

(e) Yaw moment coefficient

Figure 14. Aerodynamic modeling of Immelmann turn maneuver.

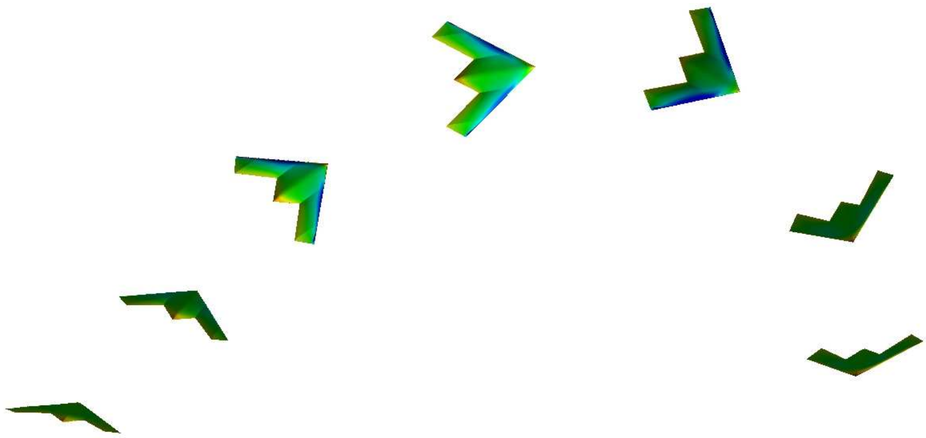

(a) Half Lazy-8.

(b) Immelmann turn.

Figure 15. Surface pressure solutions during Lazy-8 and Immelmann Turn maneuvers.